JACS
JOURNAL OF THE AMERICAN CHEMICAL SOCIETY

ARTICLE

pubs.acs.org/JACS

Nanosynthesis Routes to New Tetrahedral Crystalline Solids: Silicon-like Si_3AlP

Tylan Watkins,[†] Andrew V. G. Chizmeshya,[†] Liying Jiang,[‡] David J. Smith,[‡] Richard T. Beeler,[†] Gordon Grzybowski,[†] Christian D. Poweleit,[‡] José Menéndez,[‡] and John Kouvetakis*[,†]

[†]Department of Chemistry and Biochemistry, and [‡]Department of Physics, Arizona State University, Tempe, Arizona 85287, United States

ABSTRACT: We introduce a synthetic strategy to access functional semiconductors with general formula A_3XY (A = IV, X−Y = III−V) representing a new class within the long-sought family of group IV/III−V hybrid compounds. The method is based on molecular precursors that combine purposely designed polar/nonpolar bonding at the nanoscale, potentially allowing precise engineering of structural and optical properties, including lattice dimensions and band structure. In this Article, we demonstrate the feasibility of the proposed strategy by growing a new monocrystalline $AlPSi_3$ phase on Si substrates via tailored interactions of $P(SiH_3)_3$ and Al atoms using gas source (GS) MBE. In this case, the high affinity of Al for the P ligands leads to Si_3AlP bonding arrangements, which then confer their structure and composition to form the corresponding Si_3AlP target solid via complete elimination of H_2 at ∼500 °C. First principle simulations at the molecular and solid-state level confirm that the Si_3AlP building blocks can readily interlink with minimal distortion to produce diamond-like structures in which the P atoms are arranged on a common sublattice as third-nearest neighbors in a manner that excludes the formation of unfavorable Al−Al bonds. High-resolution XRD, XTEM, and RBS indicate that all films grown on Si(100) are tetragonally strained and fully coherent with the substrate and possess near-cubic symmetry. The Raman spectra are consistent with a growth mechanism that proceeds via full incorporation of preformed Si_3AlP tetrahedra with residual orientational disorder. Collectively, the characterization data show that the structuro-chemical compatibility between the epilayer and substrate leads to flawless integration, as expected for pseudohomoepitaxy of an Si-like material grown on a bulk Si platform.

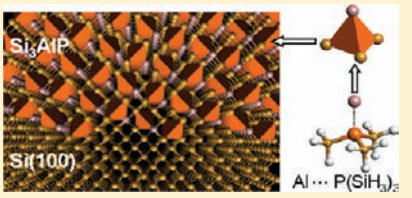

INTRODUCTION

Alloys with the general formula $(III-V)_{1-x}(IV_2)_x$ belong to a specific class of hybrid polar nonpolar materials formed by combining isolectronic molar amounts of a group IV constituent and an asymmetrical pair from the columns III and V. The chemical formula is based on the observation that both the IV and the III−V components condense as crystals described by a simple 2-atom rhombohedral cell (typically diamond and zinc-blende, respectively). Many of these materials are predicted to be direct gap semiconductors, and their wide range of band gaps and lattice constants are expected to create many application opportunities from lasers to photovoltaics. To date, only a few such IV/III−V compounds have been experimentally explored[1−6] with the common feature that the III−V and group IV components are separately delivered and allowed to react at relatively high temperatures. The material systems range from BNC_2 (a hybrid between diamond C and c-BN), which has recently been shown to exhibit hardness that rivals that of diamond,[7] to the classic $(Ge_2)_x(GaAs)_{1-x}$ alloy with a history spanning over 20 years. Optical studies of $(Ge_2)_x(GaAs)_{1-x}$ reveal a strong and asymmetric bowing in the compositional dependence of the direct band gap whose interpretation has been controversial.[8−10] Unfortunately, the elucidation of these controversies and the introduction of new families of $(III-V)_{1-x}(IV_2)_x$ materials have been hindered by the ubiquitous and perhaps expected development of phase separation under very diverse growth conditions. In the particular case of $(Ge_2)_x(GaAs)_{1-x}$, the pronounced phase separation observed under metal−organic chemical vapor deposition (MOCVD) growth conditions has precluded its use as the long-sought photovoltaic material with a band gap near 1 eV and a lattice constant close to that of Ge.[4]

STRUCTURAL AND SYNTHESIS CONCEPTS

The absence of control over the detailed bonding configurations associated with different possible structures can be linked to the limitations of the conventional synthesis strategies employed so far for $(III-V)_{1-x}(IV_2)_x$ alloys. Accordingly, in this Article, we introduce an entirely new approach to the growth of these compounds that reduces or eliminates the possibility of phase separation. This is achieved by deploying molecular growth precursors, which combine group IV and III−V atoms to form the desired building blocks of the target solid. The simplest such molecular species should contain a tetrahedral core with composition $(III-V)-(IV)_3$, incorporating a single III−V acceptor−donor pair with three group IV atoms. The experimental viability of this strategy is demonstrated by the growth of a new Si_3AlP semiconductor with state-of-the-art structural properties. In this case, 1 Al−P and 3 Si can be combined to produce a distinct tetrahedral $(Al-P)-Si_3$ unit, which once incorporated within the crystal adopts the local bonding environment of $-Si_3-Al-P-Si_3-$. From a synthesis perspective, the most potent

Received: July 19, 2011
Published: August 30, 2011

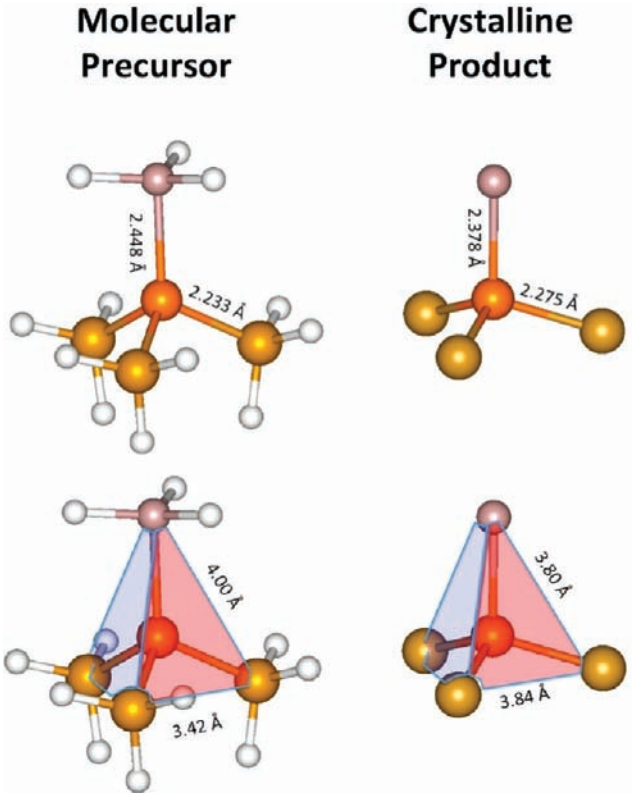

Figure 1. Comparison of the simulated structures of the Al−P−Si_3 tetrahedral units in the hypothetical molecule AlH_3:$P(SiH_3)_3$ and the corresponding core as incorporated within the crystalline environment to form the extended solid network (see text for computational details). Si, P, and Al are represented by gold, orange, and pink spheres, respectively. Note that the bond lengths and tetrahedral edge dimensions within an Al−P−Si_3 unit become more regular as the molecular adduct is incorporated into the solid via elimination of the terminal H atoms.

strategy is therefore to develop precursors that incorporate Si_3−Al−P molecular cores as shown in Figure 1. Note that only two distinct Al−P−Si_3 and P−Al−Si_3 conformations possess the structural motif and chemical makeup of the target solid. However, only the Al−P−Si_3 cluster in which the central P atom is bonded to 3 Si and 1 Al terminal species is a thermodynamically plausible bonding arrangement when viewed as an isolated molecule terminated by hydrogen atoms (see structural modes in Figure 1). The use of such molecular building blocks with preformed bonding arrangements should minimize or even completely avoid the formation of antiphase domains, atomic segregation, or energetically unfavorable bonds in the solid phase. This key feature is absent in prior synthesis strategies based on mixtures of conventional metal−organic and hydride sources. Using the design concept of conferring structure and composition in the (III−V)−$(IV)_3$ system at the molecular level, a wide range of materials can be envisioned as synthetic targets, including not only the Si_3AlP compound introduced here but also the equivalent $GaPSi_3$, Si_3BP, Ge_3GaAs, and Ge_3-GaSb relatives.

From a precursor development perspective, the isolation of the hypothetical AlH_3:$P(SiH_3)_3$ shown in Figure 1 as a stable single source compound may not be practical due to possible dissociation channels that eliminate silanes (SiH_4) under normal

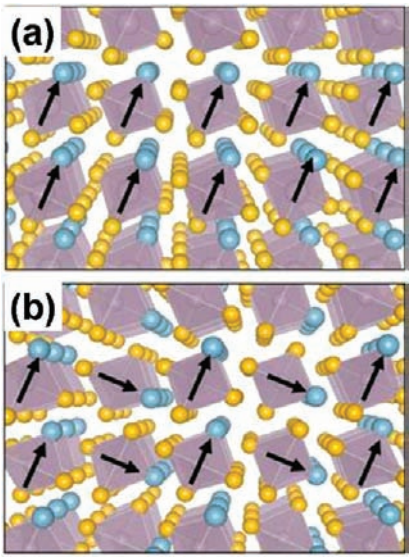

Figure 2. Polyhedral representation of the Si_3AlP crystal structure corresponding to two distinct arrangements of the $AlPSi_3$ units. The black arrows indicate the direction of the P−Al bonds.

conditions. We note that in pursuing a model adduct $AlMe_3$:$P(SiH_3)_3$ analogous to AlH_3:$P(SiH_3)_3$ by combining $P(SiH_3)_3$ and Me_3Al, we invariably obtained $(SiH_3)_2PAlMe_2$ as the stable product via elimination of $MeSiH_3$.[11] To circumvent this issue, here we adopt a more direct and highly controllable deposition approach involving thermally activated reactions between the $(H_3Si)_3P$ compound and Al atoms generated from a Knudsen cell in a gas source molecular beam epitaxy (GSMBE) chamber. The $(H_3Si)_3P$ molecule is a stable and highly volatile liquid with a significant vapor pressure of 18 Torr at 22 °C, well suited for film growth by low pressure CVD. The molecular structure consists of near tetrahedral PSi_3 cores possessing the target P/Si stoichiometry and preformed Si−P bonds that favor low-temperature reaction routes. The electron-rich P functionality has the required reactivity to readily combine with the acidic Al atoms to form Al−P bonds without any additional activation. This interaction is likely to produce an intermediate complex with "Al:$P(SiH_3)_3$" composition and tetrahedral structure according to the reaction:

$$P(SiH_3)_3(g) + Al(g) \rightarrow \text{“Al :}P(SiH_3)_3\text{”} \rightarrow Si_3AlP(s) + \frac{9}{2}H_2(g) \quad (1)$$

We have previously reported similar pathways to produce AlNSiC quaternaries via reaction of molecular SiH_3CN and Al atoms at 700 °C.[12] Under the low-temperature conditions employed in our current deposition experiments (475−500 °C), we expect the terminal Si−H bonds to be readily eliminated as H_2 to condense a crystalline solid with intact incorporation of the (Al−P)−Si_3 tetrahedron.

The proposed growth mechanism requires that the tetrahedra be interconnected without inducing energetically costly bond strains. The encapsulation of P within a 4-fold coordination sphere of three Si and one Al atoms precludes the formation of undesirable P−P bonds and limits the donor−acceptor interactions to single Al−P functionalities within the structure. Because

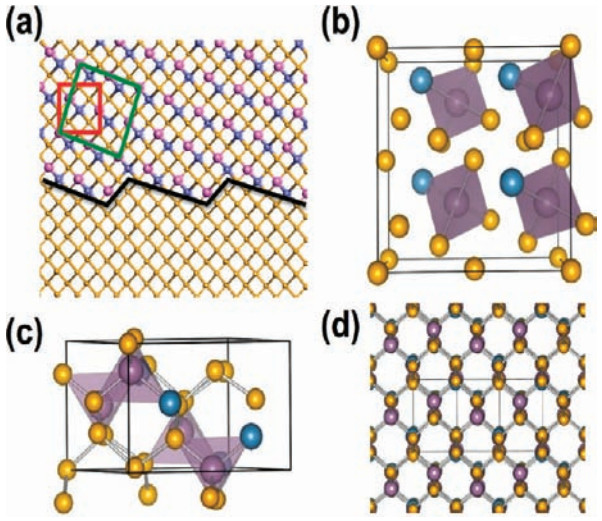

Figure 3. (a) View along the cubic (001) direction in a Si_3AlP lattice indicating the conventional crystallographic cubic cell (red) and the 20-atom Si_3AlP cell (green), with $a \times a$ and $(5/2)^{1/2}\ a \times (5/2)^{1/2}\ a$ basal dimensions, respectively. The bottom part of the image corresponds to pure Si and suggests how full Si_3AlP tetrahedra could be deposited on a Si (001) surface. (b) Primitive 20-atom cell of a hypothetical ordered phase of Si_3AlP showing the placement of Al−P−Si_3 tetrahedral units, (c) view along a direction normal to the [110] planes of a conventional diamond lattice, and (d) extended view for the latter orientation using a ball-and-stick representation. In (b)−(d), the 20-atom cell is outlined using a thin black line. Legend: Si, yellow; Al, blue; P, violet.

the tetrahedra contain 3 Si and 1 Al vertices, the formation of Al−Al bonds can also be avoided by properly orienting neighboring tetrahedra in such a way that only Si−Al bonds are formed. The resulting extended lattice contains a perfectly ordered P sublattice, where each P atom is at a third-neighbor distance from the next one. When viewed from the (001) diamond-structure direction, the P atoms are arranged in columns that form a square lattice, with each column separated by a chess Knight move from its neighbors. The arrangement of the P atoms in Si_3AlP is therefore identical to the arrangement of the C atoms in the Si_4C structure proposed by Rücker et al.[13] and related group IV analogues proposed by Crespi et al.[14] If the Al atoms are also oriented in a regular fashion, it is possible to envision several simple crystalline structures, as shown in Figure 2, where a polyhedral scheme is used to emphasize the structural relationship between building blocks. Here, the terminal Al and Si atoms are shown as blue and gold spheres respectively, while the black arrows indicate the orientation of the {P,Al} pairs within each Al−P−Si_3 tetrahedron. The simplest ordered structure, shown in Figure 2(a), consists of {P,Al} pairs oriented along a common axis. In this case, the Al atoms also form a square columnar lattice, when viewed from the (001) direction, where each column is at a Knight's move from the next one. Al atoms are at a third-neighbor distance from each other, so that the environment "seen" by Al atoms is symmetric to that seen by the P atoms. This is shown more clearly in Figure 3a. A more complex structure can be obtained by alternating the orientation of Al−P units within the rows of tetrahedra parallel to the viewing direction, as shown in Figure 2b. In this case, the P sublattice remains the same as in the first structure, whereas the columns of Al atoms, when viewed from the (001) direction, form an oblique lattice with two columns per unit cell. In this structure, some Al−Al pairs are second-neighbors, some are third-neighbors, and some are fourth-neighbors.

The relationship between the structures of Si_3AlP and the Si diamond lattice can be understood as follows. Figure 3a shows the conventional 8-atom diamond cubic cell (edge length a) and the unit cell for the Si_3AlP structure in Figure 2a. Because equivalent P or Al atoms are separated by two Knight steps, the dimensions of the Si_3AlP unit cell are $(5/2)^{1/2}\ a \times (5/2)^{1/2}\ a \times a$, so that it contains 20 atoms. This implies that each unit cell contains 4 atom-centered tetrahedra (5 atoms each), as seen in Figure 3b. Reorienting the latter cell along the conventional 110 normal of a diamond lattice shows the stacking order of the polyhedral units, as shown in Figure 3c. The resulting lattice can also be drawn using a simple ball and stick representation along a direction normal to the [110] planes, revealing the familiar "dimer row" projection of a diamond lattice (see Figure 3d). Finally, disordered variants of the structure can be generated by randomizing the Al-atom distribution, which can be accomplished while still avoiding formation of direct Al−Al bonds and preserving the perfectly ordered nature of the P sublattice. The resulting disorder of the Si and Al sublattice in actual films has implications for the Raman spectra of the solid, as discussed in subsequent sections.

MATERIALS GROWTH AND CHARACTERIZATION

The Si_3AlP films were grown directly on Si by GS MBE at 500 °C and 1×10^{-5} Torr. The container of the liquid $P(SiH_3)_3$ was connected to a gas injection manifold that was pumped to $\sim 1 \times 10^{-8}$ Torr. N-type (1−10 Ω cm) Si(100) wafers were RCA cleaned and then cleaved to a 1×1.5 cm^2 size that fits the dimensions of the sample stage. The substrates were sonicated in a series of methanol, acetone, and iso-propanol baths for 5 min each, dried under a stream of purified N_2, and inserted through a load lock into the MBE chamber at a base pressure of 3×10^{-10} Torr. The sample was then heated at 600 °C under ultra high vacuum to remove surface contaminants until the pressure inside the chamber was restored to background levels. The substrate was subsequently flashed three times to 1050 °C for 10 s to remove any remaining contaminants and to desorb the native oxide from the silicon surface. In preparation for growth, the wafer was heated to ∼500 °C, as measured by a single-color pyrometer, and the temperature was then allowed to stabilize. This temperature is considerably lower than those quoted in the aforementioned MOCVD processing of group IV/III−V alloys. The heating in our samples was performed by passing direct current though the Si substrate, yielding a uniform temperature profile.

The crystal growth was initiated by introducing the Al atoms into the chamber at flux rate of $\sim 10^{17}$ cm^{-2} s^{-1}, as measured by a quartz-crystal thickness monitor. The precursor was admitted via a nozzle located 2−3 cm away from the substrate surface. The gas flow was controlled by a needle valve at a constant rate giving a nominal 1:1 molar ratio with the Al atoms. The pressure during growth was maintained at $\sim 1 \times 10^{-5}$ Torr via dynamic pumping using a turbo pump. The typical deposition times were 1−2.5 h depending on the desired film thickness. Under these conditions, films with thicknesses in the range of 200−900 nm were produced at rates approaching 4−6 nm/min.

The samples were characterized for morphology, composition, crystal structure, and bonding properties using Rutherford backscattering (RBS), cross-sectional transmission electron

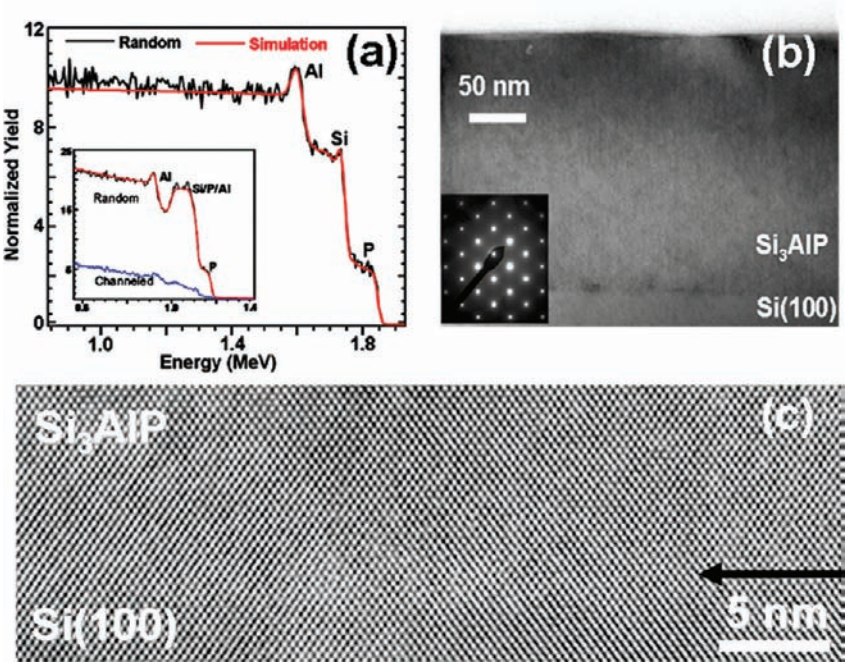

Figure 4. (a) Representative RBS spectra of Si/P/Al films. Three MeV spectrum showing well-separated P, Si, and Al signals. Fits to these data and those from a 2 MeV analogs yield an average composition of $Al_{0.9}PSi_{2.95}$ and a thickness of 190 nm. (Inset) 2 MeV spectrum of an $AlPSi_{2.90}$ film with 400 nm thickness showing a significant overlap of the RBS peaks and a remarkably high degree of channeling. (b) XTEM micrograph and diffraction pattern of the 190 nm thick sample showing a defect free layer perfectly lattice matched to Si. (c) High-resolution electron micrograph of the interface region showing a perfect commensuration between the epilayer and the substrate. The position of the interface (black arrow) was unambiguously identified using the contrast variation visible in a wider field of view image (not shown).

microscopy (XTEM), atomic force microscopy (AFM), spectroscopic ellipsometry, high-resolution X-ray diffraction (XRD), and Raman spectroscopy. The elemental content and thickness of the films were determined by random RBS. The spectra were acquired at energies of 2 and 3 MeV showing distinct, strong signals corresponding to the Al, Si, and P constituents (see Figure 4). However, as the thickness increased above 300 nm, the peaks in the 2 MeV spectra began to show a significant overlap due to the close similarity of the atomic numbers between the Si, P, and Al elements. In this case, the 3 MeV data were used to resolve the corresponding signals, thereby facilitating the quantification of the elemental contributions. For all samples grown at 500 °C, the Si and P molar ratio was consistently found to be 3:1, suggesting that the entire PSi_3 unit of the precursor was incorporated into the film structure. The corresponding Al fraction was measured to be 0.9−1, consistent with the high affinity of Al for the P ligand, only slightly lower from the expected 1:1 composition. This anomaly may be due to an instrumental (accuracy) artifact because a comparable slight deficiency in Al content was also detected by RBS in stoichiometric AlNSiC films produced using similar reaction protocols.[12] Nevertheless, the RBS analyses in this study collectively revealed an average Al/Si/P stoichiometry very close to that expected on the basis of interlinking Si_3AlP building blocks as proposed in eq 1 and Figure 2.

RBS ion channeling at 2 and 3 MeV was used to initially establish the single phase character of the material. The ratio of the aligned and random peak heights for Si, P, and Al was found to be identical in any given sample, indicating full substitutionality of the three atoms in the same tetrahedral lattice (see Figure 4a, inset). The high degree of channeling indicates near-perfect epitaxy with the underlying Si and appears more typical of a bulk crystal, suggesting that the heterostructure behaves as a continuous single unit.

Nomarski optical imaging of the layers revealed a featureless morphology devoid of any surface imperfections. This is consistent with AFM scans, which typically show an rms surface roughness of 1−3 nm for samples with thickness of 200−400 nm, respectively. The smooth morphologies are further corroborated by XTEM observations in 110 projection. The phase contrast micrographs revealed the presence of uniform layers with flat surfaces possessing thicknesses comparable to those derived from RBS and ellipsometry. Detailed analysis of the epilayer microstructure showed no threading dislocations or discernible interface defects within the field of view as illustrated by the micrograph in Figure 4b. A careful examination of the interface under high-resolution imaging as shown in Figure 4c indicates a near-perfect registry on an atomic level due to the close similarity in crystal structure and lattice dimensions between the two materials. The lattice matching is further evidenced by electron diffraction patterns obtained from the epilayer and the substrate showing a set of spots identical to that of silicon. This implies a complete overlap of the diffraction contributions as illustrated in the inset of Figure 4b. Collectively, the XTEM results show that the structuro-chemical compatibility between the film and substrate leads to seamless integration, as expected for pseudohomoepitaxy of a Si-like material grown on a bulk Si platform.

The formation of a near perfect Si_3AlP crystal under remarkably mild growth conditions is unexpected because the $P(SiH_3)_3$ starting material is typically unreactive at the low temperatures employed due to the presence of strong, multiple Si−H bonds. This observation may support the formation of $Al{:}P(SiH_3)_3$ intermediates in which the unsaturated Al centers significantly

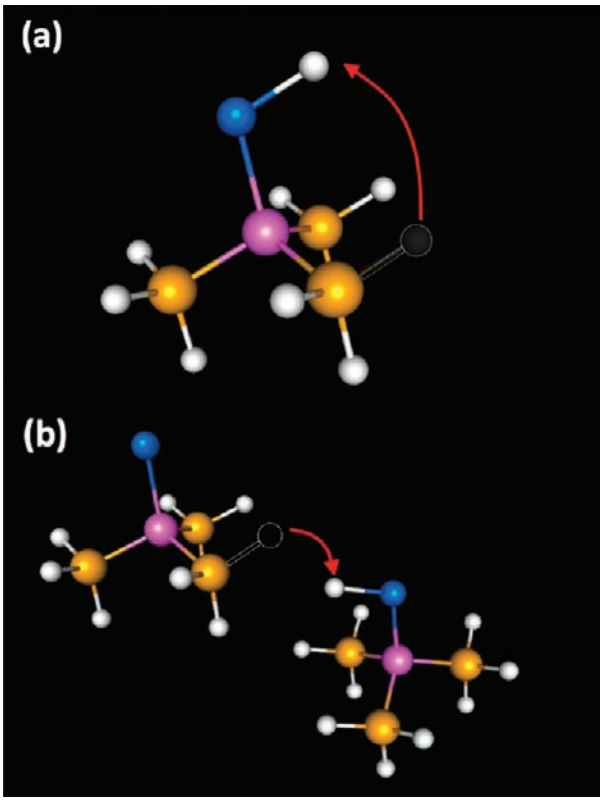

Figure 5. Schematic representation of the possible reaction mechanism for hydride elimination from intermediate Al−P(SiH_3)$_3$ clusters (legend: Si, yellow; Al, blue; P, pink).

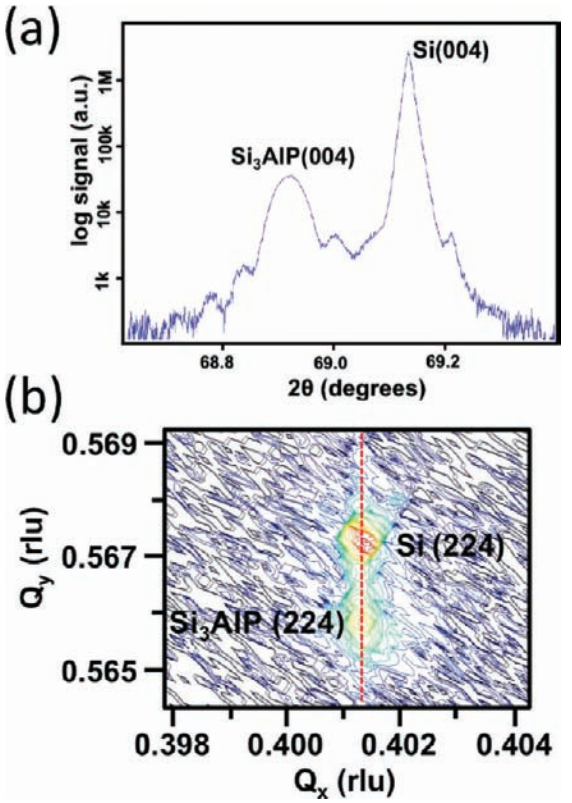

Figure 6. (a) High-resolution $\theta/2\theta$ plot showing a detailed profile of the Si_3AlP (004) reflection (adjacent to the Si counterpart) with the thickness fringes on both sides. (b) (224) reciprocal space maps showing that the Si and alloy peaks are aligned in the vertical direction (red line), which is consistent with the epilayer being fully coherent with the Si substrate.

alter the reaction mechanism, leading to the facile elimination of H_2 from the Si−H bonds. One possible scenario is that the H from the SiH_3 units is abstracted by Al to yield, for example, AlH−P(SiH_3)$_2$.SiH_2 functionalities in analogy with a β hydride-like mechanism (see Figure 5a). The resultant and relatively weak Al−H bonds significantly lower the barrier for H_2 elimination, while the remaining highly unstable silylenes (SiH_2) efficiently expel H_2, thereby circumventing the loss of silanes. Collectively, these processes ensure that the entire stoichiometry of the core is conferred to the product solid. Another perhaps more plausible (bimolecular) process for H_2 elimination may involve direct abstraction of hydrogen atoms by Al from neighboring clusters at the growth front, again leading to the formation of silylenes and subsequent crystal assembly via immediate loss of H_2 as described above (see Figure 5b).

A detailed structural analysis was conducted by high-resolution XRD to further investigate the crystallographic properties of the films including crystal orientation, lattice constants, and strain state. Using the Si substrate as an internal standard, initial $\theta/2\theta$ scans were recorded and carefully analyzed over the 20−90° range. The scans invariably contained a single reflection adjacent to the main Si (004) peak with slightly smaller *d*-spacing of 1.3614 Å, presumably corresponding to the Si_3AlP layer. No other peaks were detected in the $\theta/2\theta$ plots, corroborating the above TEM evidence that the layer is monocrystalline with the major axis oriented along the Si (004). Figure 6a shows the XRD data of the representative sample initially analyzed by TEM, as discussed above. In the vicinity of Si(004) reflection, a clearly defined Si_3AlP peak is observed possessing side maxima at left and right corresponding to thickness fringes due to interference of the beam reflected from the surface and the interface of the film. The peak is assigned to the 004 reflection and was used to calculate an out-of-plane lattice constant of 5.4456 Å. This value is slightly higher than Si (5.4306 Å) and lower than bulk AlP (5.4510 Å,[15] corresponding to an intermediate phase between the two constituents). Double crystal omega (ω) scans, taken at the 2θ position, were used to assess the crystalline quality of the film. The full width at half-maximum (fwhm) of the peaks was found to be ∼135 arc-s, which is remarkably only ∼4 times larger than that for the Si (004) peak (36.7 arc-s as determined using the same instrument), indicating that the layer is highly ordered and exhibits minimal defect densities and extremely tight crystal mosaics, as shown previously by TEM. These XRD plots of this new material in its exploratory stage bear a close resemblance to that of a highly developed, device-quality crystal, which bodes well for fast tract property characterization and potential processing from a technological perspective.

The in-plane *a* and *b* lattice parameters were measured using off-axis diffraction peaks. Strong intensity maxima corresponding to the epilayer were found in the vicinity of the (224) reflection of the substrate, which further confirms that the Si_3AlP layer possesses a near-cubic lattice structure. The (224) reciprocal space maps (ϕ = 0°) were collected, and representative plots corresponding to the substrate and the epilayers are shown in Figure 6b. Notice that the peak maxima are vertically aligned (red dotted line in Figure 6b), which indicates that the two

materials have virtually identical in-plane lattice parameters. To exclude the possibility of orthorhombic distortions, we have also measured the (−224) reciprocal space map (ϕ = 90°). The diffraction data were virtually identical for both the (224) and the (−224) reflections, yielding in-plane lattice parameters of 5.4291 and 5.4297 Å, respectively. The small discrepancy is within the error of measurement for these peaks.

Assuming that the material is cubic, the observed difference between a and c must be attributed to strain. The relaxed lattice parameter can then be obtained as $a_0 = (c + \xi a)/(1 + \xi)$, where $\xi = 2C_{12}/C_{11}$. Here, the C's are the elastic constants in the contracted index notation. For Si_3AlP, it can be estimated using the known values $\xi_{AlP} = 2C_{12}/C_{11} = 0.712$ for zincblende AlP and $\xi_{Si} = 2C_{12}/C_{11} = 0.788$ for silicon in the diamond cubic phase. A weighted average for 60% Si and 40% AlP then yields $\xi \approx 0.769$ for cubic Si_3AlP. From this analysis, we obtain a_0 = 5.4390 Å, which agrees with the Vegard average of Si and AlP. It is interesting to note, however, that while "a" was never found to be larger than that of Si, in several samples we have measured its value to be slightly smaller, between 5.42 and 5.427 Å. Tentatively, this discrepancy is attributed to nonstoichiometries involving larger than expected amounts of phosphorus in the samples. The excess P is manifested by measuring heavy n-type doping at levels as high as 5×10^{20} atoms/cm^3. These alloys exhibited somewhat broader 004 peaks, which is consistent with strain relaxation and possible defect formation. Nevertheless, their RBS spectra still showed a very high degree of channeling, in fact, comparable to that of the lattice-matched samples, indicating that the substitutionality is retained intact.

BONDING ELUCIDATION FROM SIMULATION AND RAMAN SPECTROSCOPY

First principles density functional theory calculations were conducted to study the structural and bonding properties of the new system at both the molecular and the solid-state level and compared to the experimental data. In view of the nanoscale assembly theme described above, one objective is to elucidate the structural changes associated with the incorporation of the "Al−P−Si_3" molecular units into the crystal. For this purpose, we decorated the "Al−P−Si_3" core with hydrogen atoms to form the neutral gas-phase $H_3Al-P(SiH_3)_3$ hydride molecule. The Gaussian 03 quantum chemistry package was used to obtain the optimized molecular structure at LDA level using a 6-311G++(3df,3pd) basis set. The resulting static equilibrium structure, shown in Figure 1, can be viewed as an alane-$P(SiH_3)_3$ Lewis acid complex, in which the apical angle of alane (AlH_3) unit is only slightly smaller (∼1−2°) than its isolated value, and the −P-$(SiH_3)_3$ unit adopts essentially its free molecular value. First, we see that the Al−P bond length in the crystal is compressed to the expected value relative to that in the adduct while the P−Si bond becomes slightly dilated. Together, these two effects lead to regularization of the tetrahedral cores as shown in Figure 1 where the edge lengths in the molecular core vary by more than 0.5 Å while a much smaller difference of 0.04 Å is found in the isolated core. Accordingly, the resulting crystal structure assembled from these cores is expected to adopt a diamond-like topology. Next, we investigate the properties of the solid using DFT at the LDA level using the VASP code. Ultrasoft pseudo potentials were employed to treat the [Ne] cores of the Al, Si, and P atoms with an overall energy cutoff of 400 eV. Reciprocal space integrations were carried out using a Monkhorst−Pack grid of between 20 and 40 irreducible k-points. Under these conditions, residual atomic forces and cell stress were reduced to levels below 0.01 eV/A and 0.01kbar, respectively, to yield well-converged crystalline structures close to the LDA limit.

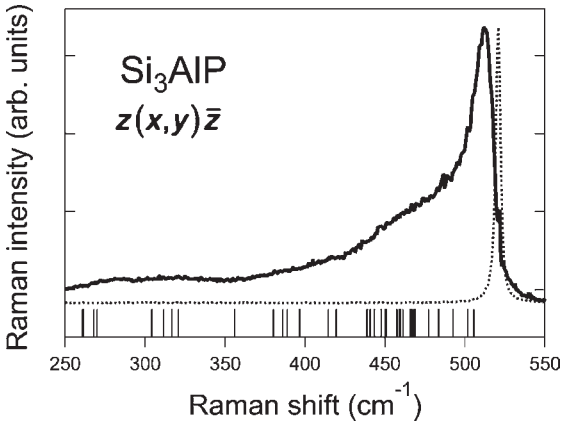

Figure 7. Solid line: Room-temperature Raman spectrum of a Si_3AlP sample after subtraction of the Si peak from the substrate. Dotted line: Room-temperature Raman spectrum from a Si reference. The excitation wavelength is 532 nm. The scattering geometry is indicated in the Porto notation, with x, y, and z as the Cartesian axes in the cubic Si cell. The bars represent calculated zone-center phonon frequencies for the ordered phase of Si_3AlP in Figure 2, rigidly upshifted to match the peak frequency.

Our initial calculations for the solid phases, presented here, correspond to the crystal in Figures 2a and 3. The fully converged equilibrium structure shows that the 20-atom primitive cell has $C1c1$ symmetry (space group no. 9) with lattice parameters a_0 = 8.523 Å, b_0 = 8.553 Å, and c_0 = 5.448 Å, and cell angles $\alpha = \beta$ = 90° and γ = 90.32° (the point group in this case is C_s) . The ground state for this simplest ordered structure is thus monoclinic, with basal dimensions a_0 and b_0 differing by ∼0.35%. This slight asymmetry is due entirely to the bias in the cell shape induced by the highly ordered arrangement of Si_3AlP units, as shown in Figure 2a. To make contact with the experimental structure, the basal dimensions can be averaged to yield a nominally tetragonal structure with $a_0^T = 8.538$ Å and $c_0^T = c_0$ = 5.448 Å, and a c/a ratio of 0.6381. The latter value is slightly different from the ideal value of 0.6325 obtained for a 20-atom diamond cubic unit cell with dimensions $(5/2)^{1/2}\, a \times (5/2)^{1/2}\, a \times a$, indicating that the relaxed equilibrium structure is expected to exhibit deviations from the cubic symmetry. The equivalent crystallographic value for the basal plane dimension, referenced to a silicon lattice, is $a_0^T/(5/2)^{1/2}$ = 5.400 Å. Adding 0.8% of this value to account for LDA's underestimate then gives a predicted value of 5.4432 Å, while the corresponding corrected value for the c-axis dimension is 5.4916 Å. A similar analysis for the structure in Figure 2b yields virtually identical estimates for the lattice constants and the degree of tetragonal distortion. The theoretically predicted c/a ratio based on these values is 1.0089 and increases to c/a = 1.013 if such a system is pseudomorphically grown on a (001) Si substrate. This appears to contradict the experimental results, which show c/a = 1.003, a ratio that was explained above in terms of epitaxial strain without invoking any intrinsic tetragonal distortion. We note, however, that the deviations from cubic symmetry predicted by simulation are likely attributable to the structural bias induced by the specific spatial arrangements of the building blocks within the nanoscale

primitive cells employed. We suspect that these deviations will be substantially reduced in a supercell simulation containing a more isotropic arrangement of $-AlPSi_3-$ units.

Strong evidence for the residual orientational disorder that might lead to an average cubic structure is obtained from the Raman spectrum of the Si_3AlP films, shown in Figure 7. The spectrum was collected in the same scattering configuration for which Raman scattering in bulk Si is allowed. It is dominated by a strong peak at 512 cm^{-1}, which is assigned to Si-like optical vibrations. This peak is asymmetrically broadened, as is the case in tetrahedral semiconductor alloys. We also see a broad feature that peaks above 450 cm^{-1} and a significant scattering background covering the entire spectral range up to the main peak. These spectral characteristics confirm that the idealized structures in Figure 2 are not obtained experimentally. On the other hand, the Raman spectrum also suggests that our Si_3AlP is considerably less disordered than the analogue $Ge_{1.2}(GaAs)_{0.4}$ alloy grown by conventional methods. The Raman spectrum of $Ge_{1.2}(GaAs)_{0.4}$ is dominated by a Ge-like feature, with a line shape similar to the Si_3AlP spectrum in Figure 7.[16] There are, however, two important differences between the two spectra. First, in the case of $Ge_{1.2}(GaAs)_{0.4}$ in ref 16, the fwhm of the main peak is 8% of its frequency, whereas in our Si_3AlP sample, the fwhm is only 4% of the peak frequency. Second, in $Ge_{1.2}(GaAs)_{0.4}$, the peak is downshifted from the Raman peak of bulk Ge by 4% of the bulk Ge frequency, whereas in our sample the equivalent downshift is only 1.7% of the bulk Si frequency. Because the force constants in tetrahedral semiconductors are very similar,[17] we would expect all shifts and widths in the two systems to be comparable when expressed as a percentage of the corresponding bulk parent material. Therefore, the observed discrepancies point to structural differences between the two systems, and the reduced width we observe could be interpreted in terms of a more ordered compound, as expected from a growth mechanism that proceeds via incorporation of preformed tetrahedra. The vertical bars at the bottom of Figure 7 show the calculated zone-center frequencies for the ordered compound in Figure 3, rigidly upshifted by 6.7 cm^{-1}, which is the difference between experimental and calculated frequencies for pure Si. We notice the presence of modes over the entire spectral range of the measurements, which explains the enhanced background relative to the Si reference. The accumulation of modes in the 450−475 cm^{-1} range matches well the broad experimental shoulder in that range, where we expect modes involving Al−P optical vibrations.[18] The highest predicted frequency is 506 cm^{-1}, somewhat below the experimental value, but this discrepancy may also be due to the use of a fully ordered 20-atom structure in the phonon calculation.

CONCLUSIONS

We have demonstrated the synthesis of a new monocrystalline semiconductor with stoichiometry Si_3AlP using a new growth strategy based on targeted interactions of $P(SiH_3)_3$ and Al atoms in a gas source MBE system. The resulting films exhibit exceptional crystallinity and, within experimental error, possess the exact composition expected from the molecular precursor. The near-perfect crystal quality is comparable to that of a typical device-quality material, which bodes well for accurate determination of the optoelectronic properties and potential development from a technological perspective. The synthetic approach followed here is applicable to other compounds with the general formula $(IV)_3-(III-V)$ and appears to be very promising for circumventing the phase separation issues that have prevented the development of alloys mixing group IV and III−V compounds.

AUTHOR INFORMATION

Corresponding Author
jkouvetakis@asu.edu

ACKNOWLEDGMENT

This work was supported by the National Science Foundation under grant DMR-0907600 and in part by the U.S. Air Force under contract DOD AFOSR FA9550-06-01-0442 (MURI program). We thank Dr. Roucka for his help with the XRD data.

REFERENCES

(1) Noreika, A. J.; Francombe, M. H. *J. Appl. Phys.* **1974**, *45*, 3690–3691.
(2) Cadien, K. C.; Eltoukhy, A. H.; Greene, J. E. *Appl. Phys. Lett.* **1981**, *38*, 773.
(3) Banerjee, I.; Chung, D. W.; Kroemer, H. *Appl. Phys. Lett.* **1985**, *46*, 494–496.
(4) Norman, A. G.; Olson, J. M.; Geisz, J. F.; Moutinho, H. R.; Mason, A.; Al-Jassim, M. M.; Vernon, S. M. *Appl. Phys. Lett.* **1999**, *74*, 1382–1385.
(5) Newman, K.; Lastras-Martinez, A.; Kramer, B.; Barnett, S.; Ray, M.; Dow, J.; Greene, J.; Raccah, P. *Phys. Rev. Lett.* **1983**, *50*, 1466–1469.
(6) Greene, J. E. *J. Vac. Sci. Technol., B* **1983**, *1*, 229.
(7) Zholozenko, V. L.; Andrault, D.; Fiquet, G.; Mezouar, M.; Rubie, D. C. *Appl. Phys. Lett.* **2001**, *78*, 1385–1387.
(8) Holloway, H.; Davis, L. *Phys. Rev. Lett.* **1984**, *53*, 1510–1514.
(9) Giorgi, G.; Schilfgaarde, M.; Korkin, A.; Yamashita, K. *Nanoscale Res. Lett.* **2010**, *5*, 469–477.
(10) McGlinn, T. C.; Klein, M. V.; Romano, L. T.; Greene, J. E. *Phys. Rev. B* **1988**, *38*, 3362–3367.
(11) Tice, J. B.; Chizmeshya, A. V. G.; Tolle, J.; Kouvetakis, J. *Dalton Trans.* **2010**, *39*, 4551–4558.
(12) Roucka, R.; Tolle, J.; Crozier, P.; Chismashya, A. V. G.; Smith, D. J.; Tsong, I. S. T.; Kouvetakis, J. *Phys. Rev. Lett.* **2002**, *88*, 206102–05.
(13) Rücker, H.; Methfessel, M.; Bugiel, E.; Osten, H. J. *Phys. Rev. Lett.* **1994**, *72*, 3578–3581.
(14) Zhang, P.; Crespi, V. H.; Chang, E.; Louie, S. G.; Cohen, M. L. *Phys. Rev. B* **2001**, *64*, 235201–10.
(15) Addamiano, A. *J. Am. Chem. Soc.* **1960**, *82*, 1537–1540.
(16) Salazar-Hernández, B.; Vidal, M. A.; Constantino, M. E. *Solid State Commun.* **1999**, *109*, 295–300.
(17) Giannozzi, P.; Gironcoli, S. d.; Pavone, P.; Baroni, S. *Phys. Rev. B* **1991**, *43*, 7231–7142.
(18) Kosobutskiĭ, A. V.; Malysheva, E. N. *Semiconductors* **2008**, *42*, 1208–1213.